Available online at www.sciencedirect.com

ScienceDirect

Materials Today: Proceedings 3S (2016) S48 – S56

materialstoday: PROCEEDINGS

5th International Conference on Functional Materials & Devices (ICFMD 2015)

Supercapacitor electrodes delivering high energy and power densities

R. Jose*, S. G. Krishnan, B. Vidyadharan, I. I. Misnon, M. Harilal, R. A. Aziz, J. Ismail, M. M. Yusoff

Nanostructured Renewable Energy Materials Laboratory, Universiti Malaysia Pahang, 26300 Kuantan, Pahang, Malaysia.

Abstract

Considerable progress has been achieved in developing supercapacitor materials with desirable charge storage properties; however, uniting energy density (E_S) and power density (P_S) in a single device is an elusive issue. We have explored diverse range of materials and structures such as (i) activated carbon from bio-resources, (ii) ceramic electrochemical materials as nanoparticles, nanowires, and nanoribbons, and (iii) layered materials to overcome this issue. An E_S of ~52.6 Wh kg^{-1} @ P_S of ~15000 W kg^{-1} is delivered using nanowire nanocomposites based device which appear to be the best ever achieved in supercapacitor charge storage mode employing aqueous alkaline electrolytes.

Selection and Peer-review under responsibility of Conference Committee Members of 5th International Conference on Functional Materials & Devices (ICFMD 2015).

Keywords: Electrospinning; Hydrothermal; Nanowire; Nanoflower; Energy storage

1. Introduction

Ever increasing demand for energy has triggered tremendous research efforts for energy storage and conversion from clean and renewable energy sources. Secondary lithium ion batteries (LIB) and supercapacitors have become

* Corresponding author. Tel.: +60169620388;
E-mail address: rjose@ump.edu.my

Selection and Peer-review under responsibility of Conference Committee Members of 5th International Conference on Functional Materials & Devices (ICFMD 2015).
doi:10.1016/j.matpr.2016.01.007

two popular protocols for energy storage devices because they are rechargeable, could be produced in diverse design with light weight and flexibility, and are easy to manufacture. The LIB provides high energy density (E_S ~150 – 200 Wh kg^{-1}) but at the expense of cycle life (<10^3 cycles) and power density (P_S ~0.5 – 1 kW kg^{-1}); whereas supercapacitors have higher P_S (2 – 10 kW kg^{-1}) and longer cycle life (10^4–10^6 cycles) but their E_S are much lower (>5 Wh kg^{-1}) [1–5]. Supercapacitors are of two types based on the energy storage mechanism, viz. (i) electrochemical double layer capacitors (EDLCs) in which a non-faradic charge accumulation occurs at a porous electrode – electrolyte interface; and (ii) pseudocapacitors (PCs), which is based on a faradic reaction at the electrode – electrolyte interface. Combination of the above two supercapacitive storage mode in a single device results in hybrid/asymmetric supercapacitors (ASCs) [6]. Allotropes and polymorphs of carbon are choice to build commercial EDLCs whereas PCs are built from ceramic nanostructures and conducting polymers. Recent reviews on supercapacitors are published elsewhere [7]. A high specific surface area of the electrode material to enable a large electrode – electrolyte interface for efficient redox reaction, high electrical conductivity to enable high rate charging and discharging, and availability of a range of energy states in the host material are the properties of a material to be selected as electrode in pseudocapacitors. Although PCs have up to 100 times higher E_S than that of EDLCs their P_S are relatively lower (<1 kW kg^{-1}) because charge transfer process between the electrode – electrolyte interface in the former is relatively slower than the charge accumulation at the interface in the later [8].

Several strategies have therefore been tested in order to achieve high E_S and P_S for oxide-based supercapacitor electrodes. For example, nanostructures of metal oxides, particularly with porous and hollow features where these materials provide much higher surface area for better electrode- electrolyte contact and short ion-diffusion length, thus enabling fast redox reaction at high rate [9–14]. An alternative method is to combine metal oxides with carbonaceous materials and/or conducting polymers for better overall electrochemical performance, since the carbon materials can improve the electric conductivity and contribute to the rate and cycling ability [15–18]. However, these methods do not change the intrinsic properties of the metal oxides.

With the above consideration, we have explored a large number of materials especially composites, layered materials in diverse morphologies and activated carbon for their application as a supercapacitor electrode. The main focus was to identify the superiority of composites and compounds over its single counterpart in electrochemical studies for supercapacitor applications. Among various morphologies and synthesis route, one dimensional nanowires synthesised by electrospinning are attractive because of its one dimensional charge transport properties.

2. Materials and Methods

2.1. Synthesis and characterization of nanostructures

Electrospinning was used to synthesize $NiCo_2O_4$, CuO, Co_3O_4 and CuO-Co_3O_4 nanocomposite nanowires and hydrothermal method was used to synthesize sodium titanate nanoflowers, MnO_2 nanorods, MnO_2 nanoflakes and $MgCo_2O_4$ nanoflowers [13,19–25]. Activated carbon was synthesised by pyrolysis method [26]. Crystal structure of the material was studied by X-ray diffraction (XRD) technique using Rigaku Miniflex II X-ray diffractometer employing Cu Kα radiation (λ = 1.5406 Å). Morphology and microstructure of the materials were studied by scanning electron microscopic technique (7800F, FESEM, JEOL, USA). High resolution lattice images and selected area diffraction patterns were obtained using transmission electron microscope (TEM) operating at 300 kV (FEI, Titan 80-300 kV).

2.2. Electrode preparation and electrochemical studies

Supercapacitor electrodes were fabricated on nickel foam substrates as described before [19]. Electrochemical properties of the electrodes were studied by cyclic voltammetry (CV), galvanostatic charge–discharge cycling, and electrochemical impedance spectroscopy in various electrolytes. The electrochemical properties in three electrode configurations were obtained at room temperature using a potentiostat galvanostat (PGSTAT M101, Metrohm Autolab B.V., Netherlands) employing NOVA 1.9 software. A platinum rod and a saturated Ag/AgCl electrode were used as the counter and the reference electrodes, respectively.

The ASCs were fabricated by assembling the CuO-Co_3O_4 nanocomposite nanowire (anode) and the AC (cathode) electrodes separated by a glass microfiber filter (fioroni) in 6 M KOH. The amount of active materials for fabrication of ASC was calculated based on the charge balance between the electrodes such that the effective capacitance at each electrode is same (See Results and Discussion section for details). A symmetric EDLC comprising of AC as both electrodes was used a control device. The capacitive properties of the ASC were obtained in two-electrode configuration at room temperature using the PGSTAT M101 potentiostat-galvanostat.

3. Results and Discussion

3.1. Morphology and Crystal structure of electrospun nanowires

Fig. 1 shows the crystal structure of materials synthesised by different methods. The lattice parameters of the materials calculated using the procedure described elsewhere [14, 16] from the XRD patterns are summarized in Table 1. Morphological details of the materials are summarised in Fig. 2. The SEM image (Fig. 2c) show that CuO-Co_3O_4 nanocomposite wires are uniform and have diameter in the range ~100 – 120 nm. However, compared to their single component counterparts, which we reported earlier, the nanocomposite nanowire has a higher diameter. The single component wires (Fig. 2b&c) were of diameter ~30 – 50 nm. The different magnification SEM images (Fig. 2d,e&h) showed flower like aggregate morphology; the formation mechanism of which could be understood as follows.

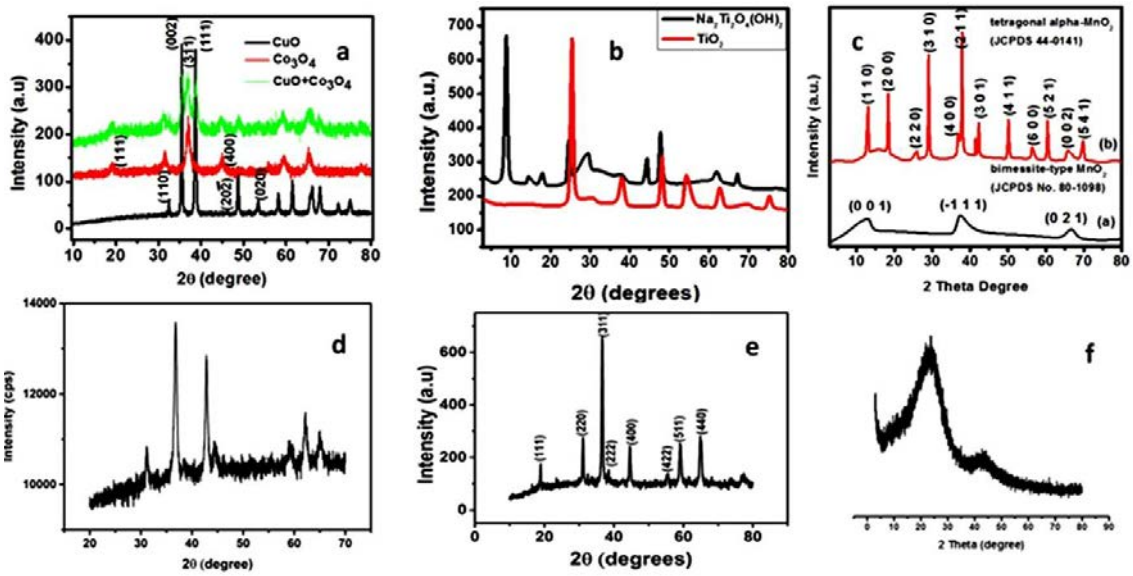

Fig. 1. XRD pattern of (a) CuO (bottom), Co_3O_4 (middle) and CuO-Co_3O_4 (top) (b) TiO_2 (bottom) and $Na_2Ti_2O_4(OH)_2$ (top); (c) α-MnO_2 (top) $NaMnO_2$ (bottom); (d)$NiCo_2O_4$;(e) $MgCo_2O_4$; (f) activated carbon.

The nanoparticles of the materials formed during hydrothermal reaction undergo delamination process and produce nanosheets. High surface-to-volume ratio of these layers makes them unstable leading their edges to curl up for releasing the excess surface energy there by forming the nanopetals. The nanosheet of each petals branched out from one another creating a floral pattern similar to a marigold or carnation. The micrometer-sized (size ~2.5 μm) nanoflower was assembled by ultrathin nanosheets growing outside from a mutual central zone of each individual spherical particles. The SEM image (Fig. 2f) showed nanorods, structures synthesised by hydrothermal process. The SEM image (Fig. 2g) shows the nanoribons of $NiCo_3O_4$ of width 120 nm synthesised by electrospinning method. Fig. 2i shows the SEM image of activated carbon synthesised by pyrolysis of palm kennel shell.

Table 1. Lattice parameters of materials obtained from XRD.

Material	Space group	Lattice parameters					
		a (Å)	b (Å)	c (Å)	α°	β°	γ°
CuO	$C12/c_1$, #15	4.598	3.46	5.135	90	99.3	90
Co_3O_4	$Fd\bar{3}m:2$	8.051	---	---	90	90	90
CuO- Co_3O_4	The two phases were chemically distinguishable and their crystal structures remained same.						
$MgCo_2O_4$	$Fd\bar{3}m:2$	8.09	---	---	90	90	90
$NiCo_2O_4$	$Fd\bar{3}m:2$	8.121			90	90	90
$Na_2Ti_2O_4(OH)_2$		18.52	3.197	2.989			
Na-MnO_2	Inter layer spacing 6.75 nm						
MnO_2	Inter layer spacing 6.77 nm						

3.2. Electrochemical Characterization of active materials

Cyclic voltammetry (CV) analysis was employed to determine electrochemical properties of supercapacitor electrodes using a three-electrode system configuration consisting of the working electrode, reference electrode, and counter electrode at various electrolytes. Fig. 3 shows the CV curves of all electrodes at various scan rates in different electrolytes. In the CV plot of the electrodes, a pair of redox peaks are seen which indicate that the origin of charge storage is reversible faradic process.

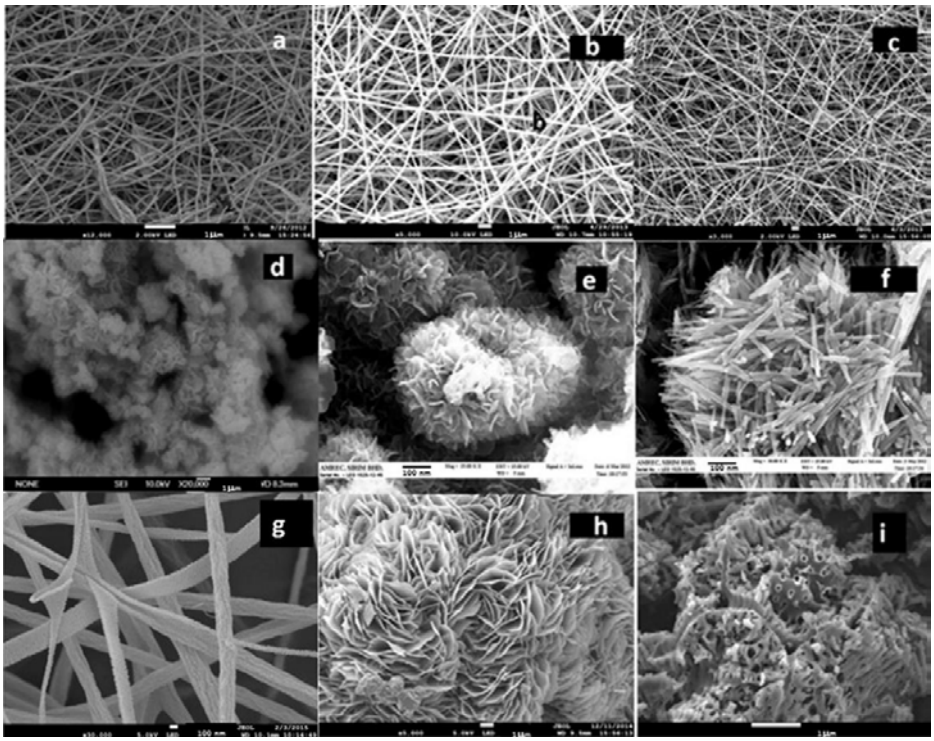

Fig. 2. SEM images of (a) CuO nanowire;(b) Co_3O_4 nanowire;(c) CuO-Co_3O_4 nanocomposite nanowire;(d) TiO_2 nanoflower; (e) $Na_2Ti_2O_4(OH)_2$ nanoflower; (f) $NaMnO_2$ nanorod; (g) $NiCo_2O_4$ nanoribons;(h) $MgCo_2O_4$ nanoflower;(i) activated carbon. The length scale is 1 μm in panels a, b, c, d, h, and i and 100 nm in panels e and f.

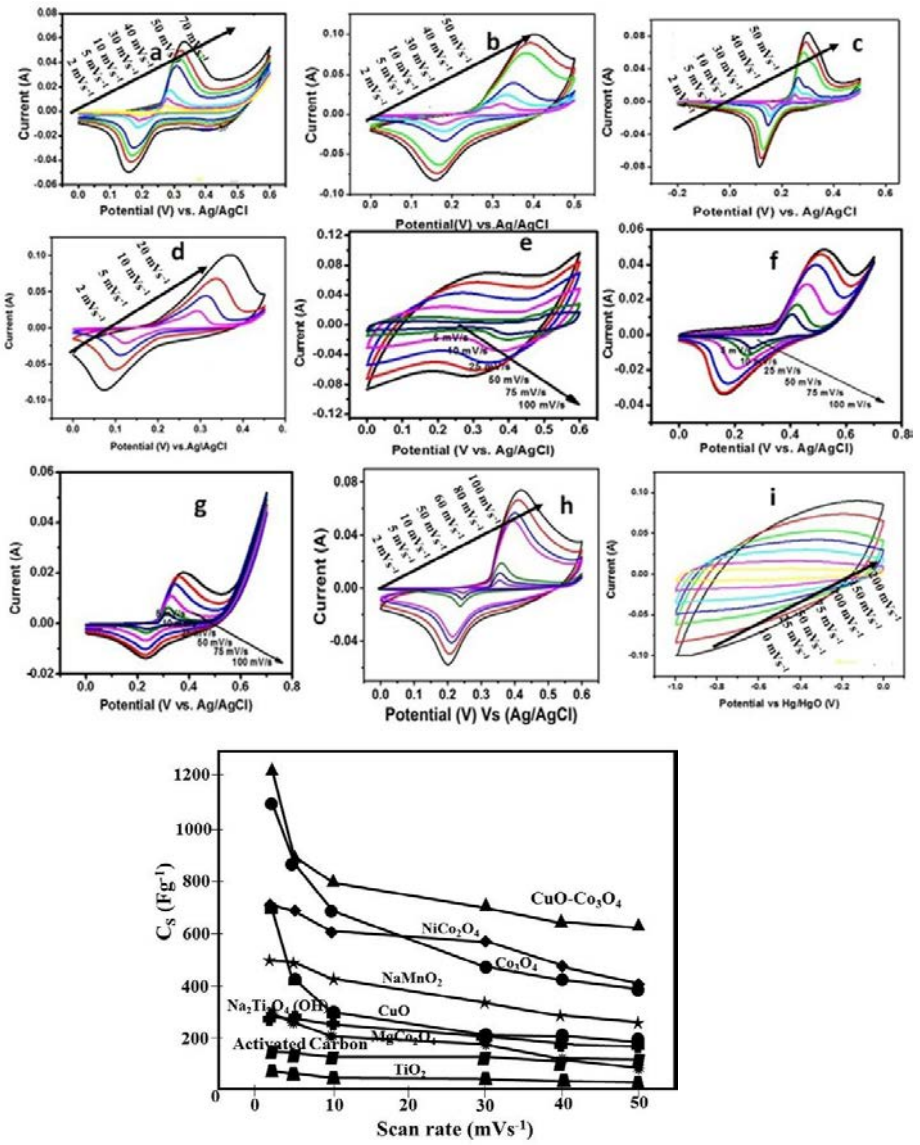

Fig. 3. The CV curves of (a) CuO nanowire in 6 M KOH;(b) Co_3O_4 nanowire in 6 M KOH; (c) CuO-Co_3O_4 nanocomposite nanowire in 6 M KOH;(d) $NiCo_2O_4$ nanoribons in 6 M KOH;(e) $NaMnO_2$ nanoflakes in 1 M LiOH;(f)$Na_2Ti_2O_4(OH)_2$ nanoflower in 1 M KOH;(g) TiO_2 nanoflower in 1 M KOH;(h) $MgCo_2O_4$ nanoflower in 3 M LiOH;(i) activated carbon in 1 M KOH. The direction of arrows are from lowest to the highest scan rate for the CV measurements. Bottom Panel: The variation C_S with scan rate for all electrodes.

The anodic peak in the CV profile shifted towards positive potentials with increase in the scan rate and the cathodic peak to the negative potential on account of the polarization in the electrode material. The asymmetric and scan rate dependent shape of the CV profiles show that the origin of the capacitance is by fast and reversible faradic reaction. The specific capacitance (C_S) of the samples measured in F g^{-1} was estimated from the cathodic part of the CV data using the equation:

$$C_S = \frac{1}{mv(E_2 - E_1)} \int_{E_1}^{E_2} i(E)dE \quad (1)$$

where E_1 and E_2 are the cutoff potentials in the CV curves and $i(E)$ is the current at each potential, $E_2 - E_1$ is the potential window, m is the mass of the active material, and v is the scan rate. The right panel of Figure 3 shows the variation of C_S with scan rate of all electrode materials. Slower scan rates enable higher diffusion of alkali cations into the nanowire electrodes thereby accessing a major fraction of the active site in the material and show high C_S. The voltammetric peak currents of the CuO-Co_3O_4 nanocomposite are higher than its constituents thereby indicating the synergistic effects owing to redox property of both material in the composite nanowire. It can be observed from the Fig. 3 that C_S of the composite electrode is approximately the sum of the C_S of its single components at higher scan rate ≥20 mV s^{-1}. This observation indicate that the constituents of the composite electrode take part in the electrochemical process individually and is in agreement with the XRD characterization that the two phases co-exist in the nanocomposite. Moreover, the C_S of the composite electrode decreases only slightly at higher scan rate, which could be attributed to the higher electrical conductivity (internal resistance of 0.8 Ω) of the composite wires achieved using CuO.

Fig. 4 shows the rate dependent charge-discharge profiles for all electrodes in various electrolytes from which usually practically available C_S of a single electrodes is calculated. The discharge curve is observed to be a combination of three processes, viz. (i) a fast initial potential drop followed by (ii) a slow potential decay, and (iii) a faster voltage drop corresponding to EDLC. The first two sections (Fig. 5) are assigned to the reduction the metal ions as observed from the CVs.

The clear non-linear shape of the discharge curves and the deviation from rectangular shape of the CV (Fig. 3) reveal that the major contribution of C_S of electrode materials originates from faradic reactions. The C_S was calculated from the charge – discharge curves using the relation

$$C_S = \frac{It}{m\Delta V} \quad (2)$$

where I, t, m and ΔV are applied current, time, active mass, and potential range of the charging and discharging events, respectively. Right panel of Fig. 4 shows the C_S calculated from galvanostatic discharge curves as a function of specific current density. The C_S decreased with increasing current density similar to that observed in the CV measurements. We can see a current density dependent behaviour in all single component electrodes whereas C_S of the composite electrode is mostly independent for current density >1 A g^{-1}.

3.3. Practical Asymmetric Supercapacitor Devices

The rationale of electrode preparation for ASCs could be found elsewhere [13]. Fig. 5a shows the CV curves of the CuO-Co_3O_4 //AC ASCs at various scan rates in 6 M KOH. The operating potential window of the CuO-Co_3O_4//AC device could be increased to 1.6 V, which is higher than that of single component devices [13,23]. The CV curves of the ASC exhibited regions with and without redox peaks characterizing pseudocapacitance and EDLC, respectively.

The cathodic and anodic currents of the CuO-Co_3O_4//AC ASC increased compared to the devices fabricated using its single components. A combination of both pseudocapacitance and EDLC was clearly observed at all scan rates. Both anodic and cathodic current increased with scan rate which indicate higher electrochemical reversibility. Oxidation peak shifted to more positive potential and cathodic peak shifted to more negative potential as observed in the three-electrode system configuration. Inset of Fig. 5a shows the variation of *Cs* with scan rate. The consistent C_S with respect to scan rate could be attributed to the improved electrical conductivity of the nanowires and would have positive impacts in their power and energy densities. Fig. 5b shows the CV curves of AC//AC symmetric EDLC at different scan rate. From the figure it can be seen that even at high scan rate, the CV curve retains a rectangular shape; indicate a pure EDLC charge storage mechanism.

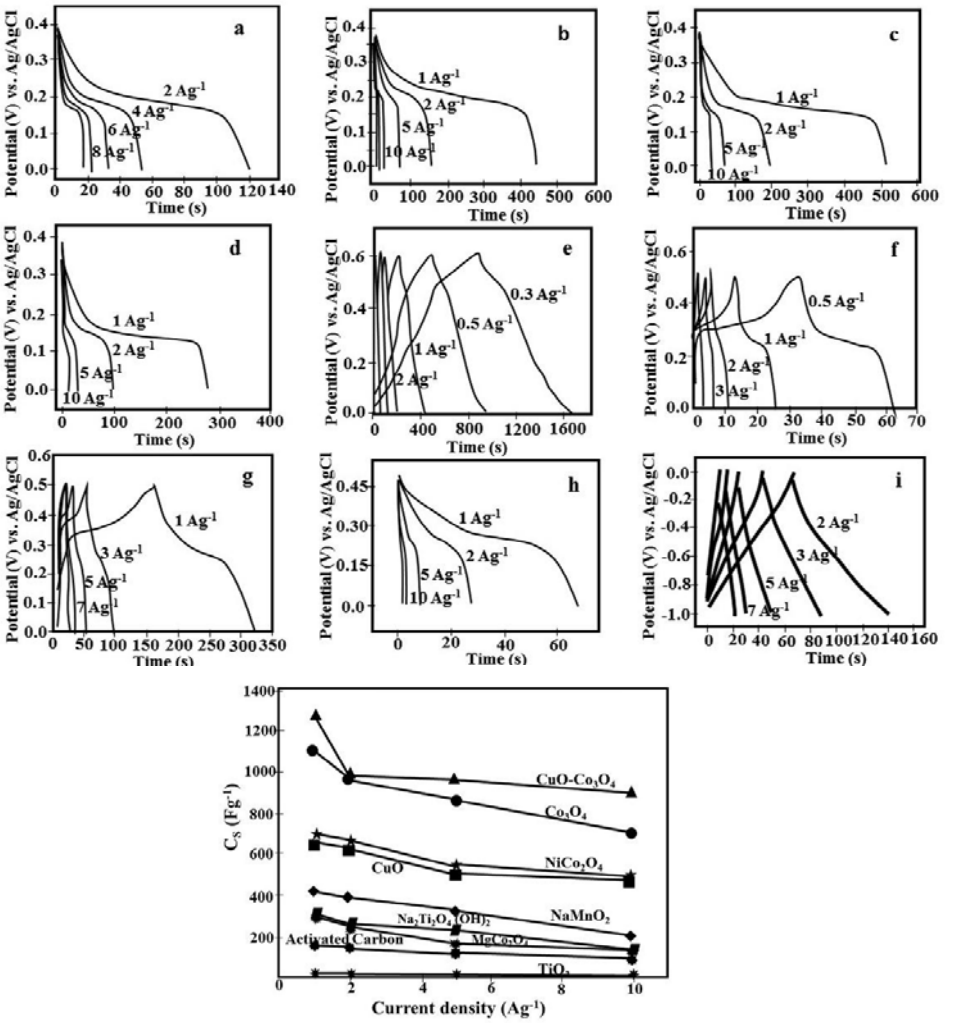

Fig. 4. Charge –discharge curves of (a) CuO nanowire in 6 M KOH;(b) Co_3O_4 nanowire in 6 M KOH;(c) CuO-Co_3O_4 nanocomposite nanowire in 6 M KOH;(d) $NiCo_2O_4$ nanowire in 6 M KOH;(e) $NaMnO_2$ nanorods in 1 M LiOH; (f) TiO_2 nanoflower in 1 M KOH;(g) $Na_2Ti_2O_4(OH)_2$ nanoflower in 1 M KOH;(h) $MgCo_2O_4$ nanoflower in 3 M LiOH;(i) activated carbon in 1 M KOH. Bottom Panel: The variation of C_S of electrode materials with current density.

To further evaluate the electrochemical performance, galvanostatic CDC was conducted at varying current densities. Fig. 5c shows the discharge curves of CuO-Co_3O_4//AC at varying current density. A higher potential window was observed for the CuO-Co_3O_4//AC ASC, consistent with that observed from the CV measurements. The nonlinear shape of the discharge curves indicates the potential dependent nature of faradic reaction. A uniform decrease in discharge time is observed with increase in current density which indicates high rate capacity of CuO-Co_3O_4 //AC asymmetric. It could be attributed to the incomplete faradic reaction due to the diffusion resistance experienced by massive OH^- ions. Inset shows the variation of C_S as a function of current density. The CuO- Co_3O_4 composite have shown good rate capability that could be attributed to higher electrical conductivity of the composite. Therefore, due to the higher V and $C_{S,}$ CuO-Co_3O_4 //AC has higher charge storage capability than the

ASCs with its single components.

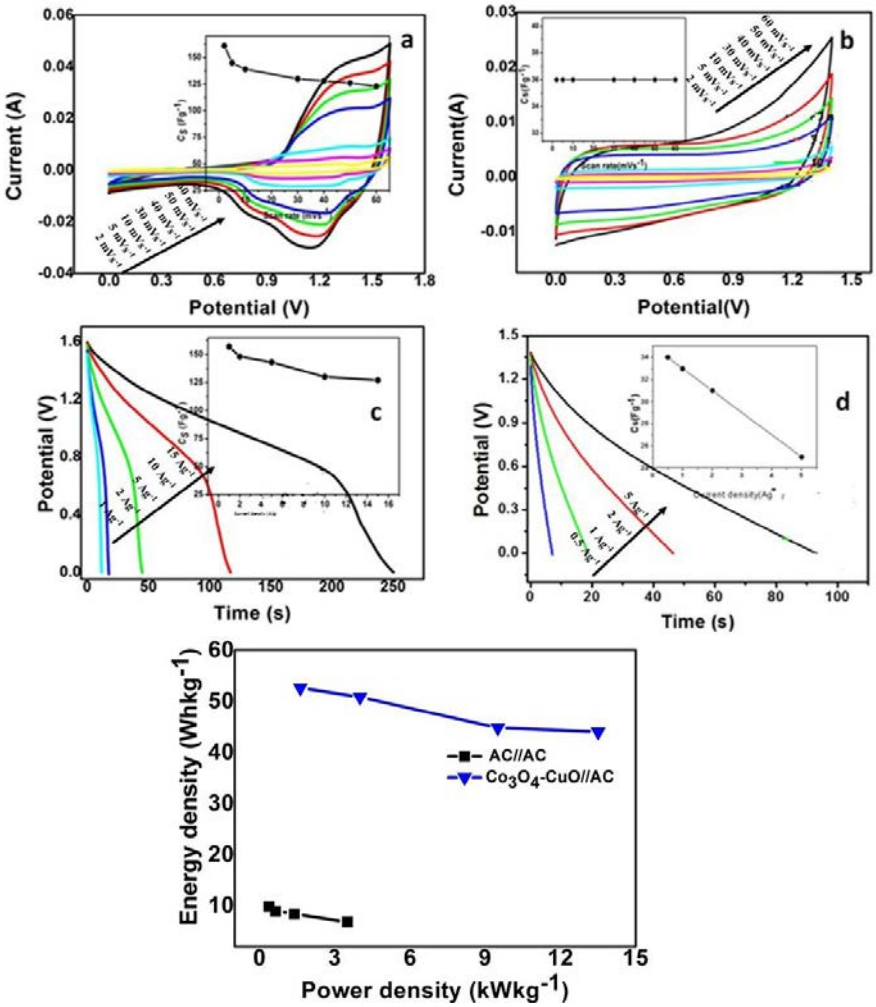

Fig. 5: (a) CV curves of CuO-Co_3O_4//AC device in 6 M KOH at various scan rate; inset shows the variation of C_S with scan rate;(b) CV curves of AC//AC in 6 M KOH at various scan rate; inset shows the variation of C_S with scan rate;(c) discharge curves of CuO-Co_3O_4 nanocomposite nanowire in 6 M KOH at various current density; inset shows the variation of C_S with current density; (d) discharge curves of AC//AC in 6 M KOH at various current density; inset shows the variation of C_S with current density. The direction of arrows are from lowest to the highest scan rate for the CV measurements. Bottom panel: Ragone plot of the device.

The E_S and P_S of the ASCs were calculated using the equations, $E_S = ½\ C_S V^2$; $P_S = E_S/\Delta t$. Right panel of Figure 5 shows the Ragone plot of all the four types of devices. The Co_3O_4-CuO//AC delivered E_S of 52.6, 50.8, 44.8 and 44 Wh kg^{-1} at P_S of 1620, 4000, 9500 and 14000 W kg^{-1}, respectively. On the other hand, performance of the control EDLC is much inferior. The EDLC delivered E_S of 9.2, 8.9, 8.4 and 6.8 Wh kg^{-1} at P_S 358, 695, 1400 and 3500 W kg^{-1}, respectively. Interestingly, in contrast to the conventional ASCs, in which the P_S is compromised for higher E_S, the P_S of the present ASC using CuO-Co_3O_4 nanowires is superior to that of the EDLC at all E_S due to the directional charge storage properties of the nanowires. In short, the E_S of the CuO-Co_3O_4//AC ACS reaches 52.6 Wh kg^{-1} at a P_S of 14000 W kg^{-1} which is six times higher than those of symmetrical AC//AC supercapacitor

(8.4 Wh kg^{-1}) at current density 2 A g^{-1}. The high power density allows the device to be charged at a faster rate; in the existing devices such faster processing stores only small amounts of charges. The device fabricated using the composite nanowires store energy as high as 52.6 Wh kg^{-1} in less than a minute's time.

Conclusions

In conclusion, we have shown that electrospun CuO-Co_3O_4 nanocomposite nanowires have improved performance than its single counterpart and activated carbon, which could be assigned to its improved electrical conductivity. The Na^+ intercalated layered structures could achieve two to three fold higher capacitances than the layered structure without Na^+ intercalation. Cyclic voltammetric measurements show that the superior electrical conductivity of CuO-Co_3O_4 nanocomposite nanowires help the electrode to achieve a high specific capacitance 1277 F g^{-1} in 6 M KOH aqueous solution with 100% Coulombic efficiency. A practical supercapacitor fabricated in asymmetric configuration using the CuO-Co_3O_4 nanocomposite nanowires as anode and activated carbon as cathode gave energy densities 52.6, 50.8, 44.8 and 44 Wh kg^{-1} at power density of 1620, 4000, 9500 and 14000 W kg^{-1}, respectively which are much superior to a control device fabricated using activated carbon as its both electrodes. High abundance of CuO and Co_3O_4 in the earth's crust and promising results achieved herewith offer unique opportunities to develop practical supercapacitors at lower costs.

Acknowledgements

This work is supported by the Research and Innovation Department (RDU 150325) of Universiti Malaysia Pahang.

References

[1] I.E. Rauda, V. Augustyn, B. Dunn, S.H. Tolbert, Acc. Chem. Res. 46 (2013) 1113.
[2] A.K. Shukla, T. Prem Kumar, Wiley Interdiscip. Rev. Energy Environ. 2 (2013) 14.
[3] G. Wang, L. Zhang, J. Zhang, Chem. Soc. Rev. 41 (2012) 797.
[4] Q. Lu, J.G. Chen, J.Q. Xiao, Angew. Chem. Int. Ed. Engl. 52 (2013) 1882.
[5] J. Jiang, Y. Li, J. Liu, X. Huang, C. Yuan, X.W. Lou, Adv. Mater. 24 (2012) 5166.
[6] B.E. Conway, in:, Kluwer Acad. Publ. NewYork, 1997.
[7] M. Zhi, C. Xiang, J. Li, M. Li, N. Wu, Nanoscale 5 (2013) 72.
[8] B.E. Conway, V. Birss, J. Wojtowicz, J. Power Sources 66 (1997) 1.
[9] X. Zhao, B.M. S, P.J. Dobson, P.S. Grant, Nanoscale (2011) 839.
[10] X. Wang, J. Liu, Y. Wang, C. Zhao, W. Zheng, Mater. Res. Bull. 52 (2014) 89.
[11] F.X. Wang, S.Y. Xiao, Y.S. Zhu, Z. Chang, C.L. Hu, Y.P. Wu, R. Holze, J. Power Sources 246 (2014) 19.
[12] M.-C. Liu, L. Kang, L.-B. Kong, C. Lu, X.-J. Ma, X.-M. Li, Y.-C. Luo, RSC Adv. 3 (2013) 6472.
[13] B. Vidyadharan, R.A. Aziz, I.I. Misnon, G.M. Anil Kumar, J. Ismail, M.M. Yusoff, R. Jose, J. Power Sources 270 (2014) 526.
[14] Y. Tang, Y. Liu, S. Yu, S. Mu, S. Xiao, Y. Zhao, F. Gao, J. Power Sources 256 (2014) 160.
[15] X. Xia, J. Tu, Y. Zhang, X. Wang, C. Gu, X. Zhao, H.J. Fan, ACS Nano (2012) 5531.
[16] W. Yang, Z. Gao, J. Ma, X. Zhang, J. Wang, J. Alloys Compd. 611 (2014) 171.
[17] A.E.A. Said, M.M.A. El-wahab, S.A. Soliman, M.N. Goda, Nanosci. Nanoeng. (2014) 17.
[18] S. He, C. Hu, H. Hou, W. Chen, J. Power Sources 246 (2014) 754.
[19] B. Vidhyadharan, N. Khayyriah, M. Zain, I.I. Misnon, R.A. Aziz, J. Ismail, M.M. Yusoff, R. Jose, J. Alloys Compd. (2014).
[20] S.G. Krishnan, M.V. Reddy, M. Harilal, B. Vidyadharan, I.I. Misnon, M.H.A. Rahim, J. Ismail, R. Jose, Electrochim. Acta 161 (2015) 312.
[21] R.A. Aziz, I.I. Misnon, K.F. Chong, M.M. Yusoff, R. Jose, Electrochim. Acta 113 (2013) 141.
[22] B. Vidyadharan, P.S. Archana, J. Ismail, M.M. Yusoff, R. Jose, RSC Adv. 5 (2015) 50087.
[23] B. Vidyadharan, I.I. Misnon, J. Ismail, M.M. Yusoff, R. Jose, J. Alloys Compd. 633 (2015) 22.
[24] B. Vidhyadharan, I.I. Misnon, R.A. Aziz, K.P. Padmasree, M.M. Yusoff, R. Jose, J. Mater. Chem. A 2, (2014) 6578-6588.
[25] A. A. Radhiyah, M. Izan Izwan, V. Baiju, C. Kwok Feng, I. Jamil, R. Jose, RSC Adv. 5 (2015) 9667.
[26] I.I. Misnon, N. Khairiyyah, M. Zain, R.A. Aziz, B. Vidyadharan, R. Jose, Electrochim. Acta 174 (2015) 78.